AALBORG UNIVERSITY

Iron phosphate glass-ceramic anodes for lithium-ion batteries

Qi, S.B.; Li, X.Y.; Yue, Yuanzheng; Zhang, Y.F.

Iron phosphate glass-ceramic anodes for lithium ion batteries

Shibin Qi[a], Xiangyu Li[a], Yuanzheng Yue[a,b], Yanfei Zhang[a,*]

[a] School of Materials Science and Engineering, Qilu University of Technology (Shandong Academy of Sciences), Jinan 250353, China

[b] Department of Chemistry and Bioscience, Aalborg University, 9220 Aalborg, Denmark

[*] Corresponding Author. E-mail: zhang-yanfei@hotmail.com (Y.Z.)

This work is devoted to celebration of the International Year of Glass.

Abstract: The oxide glass-based anodes for Lithium-ion Batteries (LiBs) still suffer from two critical drawbacks, i.e., low reversible capacity and low electrical conductivity. Here, we report a new way to overcome the two drawbacks. Specifically, we chose $50Fe_2O_3$-$50P_2O_5$ (50Fe50P) glass composition as the anode material for LiBs, and then thermally treat it at 1118 K (T_g+345 K) for 0.5 h under reducing atmosphere (5mol% H_2+95mol%Ar). The thermal reduction treatment led to formation of $Fe_2(P_4O_{12})$ and $Fe_2Fe_5(P_2O_7)_4$ crystals. The reduced glass-based anode for LiBs exhibits the capacity of 373 mA h g^{-1} after 1000 charge/discharge cycles at 1 A g^{-1}, which is higher than that of the oxidized one. The reduction treatment greatly lowers the charge transfer resistance in the glass anode, indicating the enhancement of the electrical conductivity. This performance improvement could arise from the increase of accessible active sites for Li$^+$ ion storage and transfer due to the

existence of crystal-crystal/crystal-glass boundaries, as well as from the improvement of the electron transfer between Fe^{2+} and Fe^{3+} during cycling. This reduction-crystallization approach could help develop high-performance oxide glass-ceramics based anodes for advanced LiBs.

Key Words: Iron phosphate glass; Crystallization; Reducing condition; Anode; Lithium ion battery

1. Introduction

As the increasing demand for sustainable and renewable energy sources to replace the fossil fuels, battery materials and technologies are being investigated in full swing, such as lithium/sodium/zinc ion batteries[1-3], lithium-air battery[4], lithium-sulfur battery[5], zinc-air battery[6] and all solid-state battery[7]. Nevertheless, Li-ion batteries (LiBs) are still by far the commercially applied ones in the areas of electronics and automobiles. To improve the LiB performances, it is important to ensure the superior properties of anode materials[8]. Currently, the most common rechargeable Li-ion battery is based on graphite anodes due to its flat and low working potential relative to lithium, low cost and excellent cycle life[9]. However, both the low theoretical capacity and the low diffusion rate of lithium ions into graphite are not sufficiently high for meeting the level required by various electric vehicles and smart grids[9]. Therefore, it is crucial to develop high performance anode materials to replace graphite in lithium-ion batteries (LiBs).

Oxide glasses severing as anode materials for LiBs have recently aroused considerable interest of battery scientists owing to their unique 3D network structure[10-14]. The open

network structure and absence of grain boundaries of the glasses can effectively buffer the strain/stress induced by lithiation/delithiation, ensuring the stable charge/discharge cycling performance of LiBs[13]. Nonetheless, one of the main drawbacks of oxide glasses anodes is their low electric conductivity, i.e., slow transfer kinetics of electrons and Li^+ ions. To overcome this problem, many efforts have been made, such as reducing the multivalent metal ions to the low-valence state in glass[12,15]. According to the "small polaron hopping" conduction mechanism[16], the electron conductivity of oxide glasses with multivalent metal ions mostly comes from the electron hopping from low to high valance sites. Therefore, the content of low-valence metal ions plays a critical role in improving the electrical conductivity of the semiconducting glass. Du et al.[12] report that the V_2O_5-P_2O_5 glass synthesized in a reducing atmosphere exhibits superior electrochemical properties to the one prepared in atmospheric air because of the increased content of low-valence vanadium ions. In addition, Ei-Desoky's group studied the effect of sulfur addition on the transport properties of semiconducting iron phosphate glasses[15]. They found that the Fe^{2+}/Fe^{3+} ratio increased with the increasing sulfur content, leading to an increased electrical conductivity. Somewhat similarly, Seung-Su Lee et al[17] prepared the nanostructured Si-based composites to reduce waste glass powder using Mg powder, which exhibited much better electrochemical performances than the pure waste glass.

In addition, the electrical conductivity of glasses can also be improved by thermal induced crystallization process[18-20]. A recent work of some of the present authors[18] demonstrated that the   reversible capacity of $50Fe_2O_3$-$50P_2O_5$ glass anode for LiBs was

enhanced by 1.5 times after 1000 cycles at the current density of 1 A g^{-1} due to formation of

Fe$_3$(P$_2$O$_7$)$_2$ crystals. This enhancement in capacity is mainly attributed to the

crystallization-induced increase of electronic conductivity. Difference from pure glass, glass

ceramics possess a large amount of boundaries between crystals and glass matrix. These

boundaries not only benefit the contact between the glass-ceramics-based anode and the

electrolyte, but also provide more active sites for storage of Li$^+$ ions. Moreover, the glass

phase in the anode can stand the structural changes induced by the insertion/extraction of Li$^+$

ions.

Given the above-mentioned aspects, in this work we investigated the crystallization

behavior of 50Fe$_2$O$_3$-50P$_2$O$_5$ (50Fe50P) glass under reducing atmosphere and its effect on the

anode performances for LiBs. The electrochemical performances of 50Fe50P glass[18] was

compared with those of the 50Fe50P glass ceramics produced in atmospheric air and under

the reducing condition (i.e., 5mol% H$_2$+95mol%Ar), respectively. The reduced 50Fe50P

glass ceramics exhibited the largest reversible capacity, best rate capability and lowest charge

transfer resistance compared to both 50Fe50P glass and the glass ceramics prepared in

atmospheric air. We discussed the microstructural origin of the difference in electrochemical

performances among the three anode materials.

2. Experimental section

2.1 Preparation of Glass and Glass Ceramics

We chose and prepared the $50Fe_2O_3$-$50P_2O_5$ (50Fe50P) glass as anode material for LiBs by using the melt-quenching method[18]. 50Fe50P glass was milled in an agate mortar for 0.5h to prepare the powder. Figure 1 shows the particle size distribution of the glass powder, which are displayed as the volume of powder and the cumulative volume distribution. The size distribution is in the range from about 0.1 to 25 μm with a D50 (diameter at 50% cumulative volume) of 1.4 μm. Glass powders were heated at 5 K/min to 1118 K in air and 5 mol% H_2+95 mol% Ar, respectively, in a tube furnace and kept for different time. After treatment, the glass powders were cooled down to room temperature in the furnace naturally. The treatment temperature was 1118 K on the basis of the DSC results. The choice of this temperature was explained in Figure 2a. The final samples were marked according to their preparation condition, e.g., R-0.5h refers to 50Fe50P glass treated at 1118 K for 0.5 h under reducing atmosphere.

2.2 Material Characterization

The crystalline phases in samples were identified by X-ray Diffractometer (XRD, Shimadzu LabX XRD-6100, CuKα radiation) in the range of 2θ from 10-70° with a 2θ step of 0.02° per second. Differential scanning calorimetry (DSC) (Netszch Jupiter STA 449F3) was used to determine the thermal events of both the glass and glass ceramics at a heating rate of 20 K/min in a N_2 atmosphere. X-ray photoelectron spectroscopy (XPS) measurements

5

were carried out with an ESCALAB 250Xi spectrometer (ThermoFisher Scientific, USA) to determine the valence states of the sample. The field emission scanning electron microscope (FE-SEM, ZEISS GeminiSEM500) was employed for microstructure observations at etched section of the resultant glass ceramics with a plate shape by immersion in 40 vol.% HF solution for 30 seconds in order to observe clearly the morphology of crystals. The bulk glass ceramics were prepared under the same heat treatment condition to the powders. For the electrical measurements, the samples with a flat surface of roughly 0.55 cm in diameter and a thickness of 0.15 cm were prepared. Silver layers were coated on the surface of the sample. The electrical conductivities of the samples were measured by a direct current high voltage supply source (Keithley 6517B) at temperatures between 303 and 450 K.

2.3 Cell Assembly and Electrochemical Measurements

The electrochemical performances of the as-prepared glass and glass-ceramics as anode materials were evaluated using CR2032 coin cells with lithium foil (diameter of 10 mm) as the counter/reference electrode. The assembly of the battery and the electrochemical performance measurement are performed based on previous works[10, 21-23]. The charge/discharge performance and cycling stability of the batteries were tested by a Land battery test system (CT2001A) at different current densities. Both cyclic voltammetry (CV) and Electrochemical impedance spectroscopy (EIS) were performed using an electrochemical workstation (PARSTAT 3000A DX). CV curves were acquired in the voltage range of 0.01-3V, and EIS was tested in the frequency range of 100 kHz to 0.1 Hz.

3. Results and Discussion

Figure 2a shows the 20 K/min DSC upscan curves of both the as-produced 50Fe50P glass and the 50Fe50P glass-ceramics that were prepared by heat-treatment of 50Fe50P glass at 1118 K for 0.5 hour under the oxidizing and the reducing conditions, respectively. It is seen that 50Fe50P glass has a glass transition peak with T_g=773 K, followed by a sharp crystallization peak with the onset temperature of 980 K, which indicates a strong tendency of the glass to crystallization[18]. With increasing the upscaning temperature, two endothermic peaks related to melting of crystals appear at 1118 and 1250 K, respectively, suggesting the complex crystallization behavior of 50Fe50P. That is to say, the sharp crystallization peak in DSC curve might be associated with the formation of at least two crystal phases[18,20,24]. In this work, the heat treatment temperature is chosen as 1118 K owing to the following two aspects. On one hand, the glass ceramics with a main crystal phase is expected to be obtained by melting some byproduct crystals in order to clearly study the effect of crystallization on the electrochemical performances. On the other hand, such a high temperature of 1118 K corresponds to a low viscosity which favors the reduction of Fe^{3+} to Fe^{2+} ions under reducing atmosphere. For both A-0.5h and R-0.5h samples, no glass transition peaks appear in their DSC curves anymore. Instead, a melting peak appears at almost the same temperature of 1118 K, implying that most of the glass phases transform into crystals. This is confirmed by the XRD patterns of A-0.5h and R-0.5h (Figure 2b). The as-produced 50Fe50P glass is fully amorphous[18]. The identity of the crystalline phases is strongly affected by the heat-treating atmosphere. Under oxidizing condition, only one crystal phase of $Fe_3(P_2O_7)_2$ (JCPDS

80-2315) forms, and this behavior is similar to that of the 50Fe50P glass treated at 1033 or 1063 K for 4 hours [18]. On contrary, two different types of crystals, i.e., $Fe_2(P_4O_{12})$ (JCPDS 78-2285) and $Fe(III)_2Fe(II)_5(P_2O_7)_4$ (JCPDS 77-0851) form in the reduced sample.

The microstructural evolution of these two glass ceramics revealed a significant influence of the heat treatment atmosphere as is evident by the typical SEM images of A-0.5h and R-0.5h (Figures 2c and d). A-0.5h sample has granular morphologies with the uniform particle size of about 0.2 μm interspersed between the remaining glass phases. The regularly arranged prismatic crystals were observed in R-0.5h, showing the characteristic of orientational crystallization, i.e., vertically well-aligned prismatic crystals. In addition, certain irregular voids can be found among the precipitated crystals due to the etched glass phases. This implies that there is still remaining glass phases in both oxidized and reduced samples even no glass transition peaks appear in their DSC curves. In addition, the crystal structure of $Fe_2(P_4O_{12})$ was reported to be built up of two kinds of distinct FeO_6 octahedrons and two PO_4 tetrahedra, preferentially in spherical small particles[25]. Therefore, some small particles that grow on the surface of prismatic crystals (Figure 2d) might be attributed to $Fe_2(P_4O_{12})$ crystals. The integrity of these two crystals was easily noticed. The oxidized and the reduced glass-ceramics have different morphologies that could lead to different electrochemical performances if both are used as anode materials for LiBs.

Figure 2e shows the Fe 2p spectra of R-0.5h sample, in which the Fe $2p_{3/2}$ and Fe $2p_{1/2}$ peaks locate at 711.5 and 724.2 eV, respectively[26]. Due to the asymmetry features of the two peaks, the spectrum is deconvoluted into four bands at 710.7, 724.1, 716.3 and 724.8 eV,

respectively. The former two bands are attributed to Fe^{2+}. While the latter ones correspond to Fe^{3+}. This implies that although the as-received 50Fe50P glass is treated in reducing atmosphere (5 mol% H^2+95 mol% Ar), not all the Fe^{3+} ions were reduced to Fe^{2+}. According to the chemical formula, the crystal $Fe_2(P_4O_{12})$ contains only Fe^{2+} ions while both Fe^{3+} and Fe^{2+} ions exist in $Fe_2Fe_5(P_2O_7)_4$ crystal. In addition, Fe^{3+} ions might also exist in the remaining glass matrix. Therefore, it is concluded that the existence of the pairs of Fe^{2+} and Fe^{3+} in R-0.5h glass ceramics will contribute to the electrical conductivity.

The electrochemical performances of the three derived 50Fe50P samples were determined using the galvanostatic charge/discharge cycling method, electrochemical impedance spectroscopy and cyclic voltammetry. Figure 3a shows the cycling performances of the three anodes at a current density of 1 A g^{-1} and the coulomb efficiency (CE) of R-0.5h based anode. Like most of oxide glass-based anodes[10-13], all the three anodes exhibit fairly large initial reversible capacities. However, the capacities drop drastically to about 45 cycles with a value of 122, 148 and 206 mA h g^{-1} for 50Fe50P, A-0.5h, R-0.5h, respectively, then increase and keep stable until 1000 cycles. Take R-0.5h for an example, the first cycle showed discharge and charge capacities of 797.1 and 396.4 mA h g^{-1}, respectively, corresponding to an initial CE of 49.7%. Noted that the irreversible capacity loss during the first several cycle could be attributed to the inevitable formation of the SEI film and the irreversible reactions between the inserted Li^+ ions and glass/glass ceramics[10,13]. Afterwards, the capacity gradually increases with cycling and keeps stable until 1000 cycles. Impressively, the remaining capacity of R-0.5h anode reaches up to the largest value of 373 mA h g^{-1} at the end

of 1000 cycles, which achieves more than 200% increase of that exhibited by 50Fe50P glass

anode (150 mA h g^{-1}). Furthermore, the capacity of R-0.5h anode is also much larger than

that of A-0.5h (213 mA h g^{-1}). The coulombic efficiency of R-0.5h from the 45th to the 1000th

cycle is nearly 100% with excellent cycling stability.

Figure 3b displays the rate capacities to the three anodes at different current densities. At

the initial low current density of 0.5 A g^{-1}, the discharge specific capacity of R-0.5h reach

429.7 mA h g^{-1} in the second cycle (the initial value is not shown due to the too large value of

821.3 mA h g^{-1}) and around 257 mA h g^{-1} at the end of 20 cycles. Beyond that, the ideal

discharge specific capacity attains 218.2, 215.9 and 186.7 mA h g^{-1} at the current densities of

0.8, 1, and 2 A g^{-1}, respectively. Additionally, the discharge specific capacity is recovered to

272 mA h g^{-1} at the end of 20 cycles when the current density returns from 2 A g^{-1} to 0.5 A

g^{-1}, suggesting that R-0.5h anode has superior rate capacity. The superior cycling

performance of the R-0.5h anode could be attributed to the well-constructed microstructure

during the reducing heat-treatment. The electrochemical impedance results for 50Fe50P,

A-0.5h and R-0.5h anodes are compared in Figure 3c. The Nyquist plot of each sample

exhibits a depressed semicircle in the high frequency region and an inclined line in the low

frequency region[27,28]. The diameter of the semicircle is associated with the SEI resistance

and the charge-transfer resistance. The inclined line is assigned to the Warburg impedance,

which is related to the coefficient of Li$^+$ ion diffusion into the bulk anode. The inset in Figure

3c is the equivalent circuit used to fitting the Nyquist plots of impedance spectra. In the

equivalent circuit, R1 represents the resistance of electrolyte, corresponding to the

intersection of the semicircle at the real axis in the high frequency region. R2 and CPE1 are the resistance and capacitance, respectively, of the SEI films formed on the electrode. Rct and CPE2 represent the charge-transfer resistance and the double layer capacitance, respectively [29]. The cell with R-0.5h exhibits the SEI and charge-transfer resistances (R2 and Rct) of 0.0001 and 76.98 Ω, respectively, which are apparently lower than those of the cell with A-0.5h (70.12 and 329.6 Ω) and 50Fe50P (208.4 and 708.2 Ω). These results confirmed that the heat treatment of 50Fe50P under reducing atmosphere can ensure efficient electron and ion transportation. That is, R-0.5h exhibits the lowest charge transfer resistance than the other two samples. As is known, the charge transfer resistance is associated with complex reaction process of charge transfer between the electrolyte and the electrodes [30, 31]. Another inset of Figure 3c shows the temperature dependence of electrical conductivity (log σ) for 50Fe50P, A-0.5h and R-0.5h, respectively. All the three samples display a linear increase in electrical conductivity with temperature. Consistent with the EIS result, R-0.5h possesses the largest electrical conductivity, which increased by almost one order of magnitude compared to that of 50Fe50P. This implies that treating the 50Fe50P glass under reducing condition could be an effective way to increase the electronic conductivity.

Figure 3d shows the cyclic voltammetry (CV) curves of R-0.5h anode recorded at a scan rate of 0.1 mV s^{-1} in the voltage range of 0.01-3.0 V. The first cycle has a quite different peak from the other cycles at 0.54 V in the cathodic scan, which is attributed to the side reaction and the formation of SEI layer from the electrochemical reduction of the electrolyte. Except for the first charge/discharge cycle, there is a reduction peak at around 1.58 V. From cycle 1

to 5, the reduction peak gradually shifts to a lower voltage of 1.45V, indicating that the polarization reaction of the anode material is decreasing during the charge/discharge cycling. Moreover, the reactions between the Li^+ ions and the anode material become easier. In the oxidation scans, a broad peak near 2.27 V was observed in all the cathodic scans. Note that there is only a single couple of redox peaks in each CV curve, indicating that the insertion/extraction process of Li^+ ions is relatively simple. In addition, the inset of Figure 3d shows stable charge/discharge curves of the R-0.5h based anode at a current density of 1 A g^{-1} with identical profile, implying its high reaction activity. A discharge plateau at around 0.65 V is observed which is nearly well matched with the CV result.

To explore the origin of the enhanced capacity of R-0.5h anode from the microstructural aspect, Figure 4a shows the XRD patterns of the reduced sample before and after 1000 cycles at the current density of 1 A g^{-1}. Strikingly, there are no Bragg diffraction peaks for the reduced sample-based anode after 1000 cycles, implying that the crystal phases transform into amorphous phase upon lithiation/delithiation process. That is, the order-disorder transition occurs in R-0.5h anode during the charge/discharge cycles[27]. Furthermore, the DSC curve of the reduced anode after cycles further confirms the occurrence of order-disorder transition (Figure 4b). In the DSC curve of R-0.5h anode after cycles, two exothermic peaks appear at 740 and 895 K, which could be due to two crystallization events. The endothermic peak at 1059 K is attributed to the melting of crystals. Contrariwise, there is only an endothermic melting peak at 1123 K in the DSC curve of R-0.5h. It is worth noting that no glass transition peak occurs in the DSC curve of R-0.5h after 1000 cycles, implying

the amorphous rather than glass state of R-0.5h after cycles. Figures 4c and d show the SEM

images of R-0.5h (ball milled for 4 h at the rotation speed of 400 rpm/min) and that after

1000 cycles. It can be seen that R-0.5 h is composed of particles with a broad size distribution

in micron size. The particles have smooth surfaces and irregular shapes. As is known, the

insertion/extraction of Li^+ ions will generate a certain amount of structure stress and volume

changes on the host material, especially for the insertion of a large amount of Li^+ ions[32]. As

shown in Figure 4d, the particles of R-0.5h were transformed into very smooth microspheres

after cycling and these nanoparticles aggregated with each other. The formed nanoparticles

with larger interface areas will not only increase the contact area with the electrolyte but also

provide numerous structural defects/active sites to accommodate more Li^+ ions.

The effect of treating time (t_a) on the electrochemical performance of the 50Fe50P glass

treated at 1118 K under reducing atmosphere was evaluated by Galvanostatic

charge/discharge tests. Figure 5a shows the cycling performances for 50Fe50P, R-0.16h,

R-0.5h and R-4h, respectively, at the same current density of 1 A g^{-1}. Among the four

samples, the R-0.5h delivered the largest capacity at the end of 1000 cycles (see the inset of

Figure 5a) although all samples exhibit stable cycling performance. Figure 5b displays the

Nyquist plots for the 50Fe50P, R-0.16h, R-0.5h and R-4h anodes before cycles. It is known

that both the storage capacity and rate capability are strongly dependent on Li^+ ions diffusion

kinetics between the electrolyte and the electrode interface[33]. The R-0.5h cell shows the EIS

spectra with the smallest diameter of the semicircle, indicating the lowest charge transfer

resistance during cycling among the four anodes. This result can be explained in terms of the

structural evolution of 50Fe50P glass treated under reducing atmosphere. As shown in Figure 6, the Bragg peaks in the XRD pattern of 50Fe50P becomes stronger with the increasing t_a, indicating the increasing number of crystals. With the increasing t_a to 0.5 h, the increased number of crystals will lead to an increase of the specific surface areas accordingly, which thus provides more active sites for lithium storge and consequently the increase in capacity. Moreover, as the number of crystals increases, the interfacial regions between crystalline and the glass phases become narrower[20,34-36], resulting in the improvement in the conduction channels for hoping from Fe^{2+} to Fe^{3+} ions. This is responsible for the enhanced electrical conductivity in 50Fe50P with the increasing t_a to 0.5 h. However, when t_a is extended to 4 h, both the amount and the average size of the crystals increase, leading to the decrease of the interfacial regions, and thereby, to lowering the number of conduction paths. The large crystals in the reduced sample in turn lead to the decrease of the surface areas, and hence, of the capacity. Therefore, the optimal heat-treatment duration of 50Fe50P is 0.5 hour to achieve the superior electrochemical performance.

According to the above results, the reduced glass-ceramic-based anode exhibits the best lithium-storage performance. The improvement of the electrochemical performances of R-0.5h was attributed to the following three interdependent factors. The first is the increased electrical conductivity and the formation of well-conducting regions along the glass-crystallites interfaces. The second is the increased interface areas between crystals and glass matrix, which facilitate the contact between the anode material and the electrolyte, and provide active sites for lithium storage. The third is the remaining glass matrix in R-0.5h

anode, which avoids lattice stress and provides open vacancies for faster Li^+ diffusion, and thereby improve the reversible capacity and the structural stability.

4. Conclusion

The crystallization behaviors of the $50Fe_2O_3$-$50P_2O_5$ glass were investigated upon heat-treatment under the oxidizing and the reducing conditions, respectively. The oxidizing heat-treatment leads to formation of the $Fe_3(P_2O_7)_2$ crystals with granular morphologies, while the reducing heat-treatment results in formation of the well-aligned prismatic $Fe_2Fe_5(P_2O_7)_4$ crystals, on the surface of which there are some smaller spherical $Fe_2(P_4O_{12})$ crystals.

The reduced glass-ceramic-based anode exhibits the capacity of 373 mA h g^{-1} after 1000 cycles at the current density of 1 A g^{-1}, whereas the oxidized glass-ceramic-based ones feature the capacity of 213 mA h g^{-1} at the same current density. In addition, the reduced glass-ceramic-based anode features a significantly higher rate capability compared to both the untreated one and the oxidized one. The reduction-caused enhancement of the electrical conductivity has the following implications: (i) the concentration of Fe^{2+}-Fe^{3+} pairs is increased, and (ii) the conduction channels in the formed glass ceramics are modified in favor of the hoping from Fe^{2+} to Fe^{3+}. In addition to the iron-containing glasses, other types of transition metal containing oxide glasses could be employed to develop high-performance anodes for LiBs via reducing heat-treatment strategy.

15

References:

[1] Lu LG, Han XB, Li JQ, Hua JF, Ouyang M. A review on the key issues for lithium-ion battery management in electric vehicles. J Power Sources. 2013;226: 272-88.

[2] Yang C, Xin S, Mai LQ, You Y. Materials design for high-safety sodium-ion battery. Adv. Energy Mater. 2020; 2000974.

[3] Zhang Y, Wan F, Huang S, Wang S, Niu ZQ, Chen J. A chemically self-charging aqueous zinc-ion battery. Nat Commun. 2020;11:2199.

[4] Aurbach D, McCloskey BD, Nazar LF, Bruce PG. Advances in understanding mechanisms underpinning lithium-air batteries. Nat Energy.2016;1:16128.

[5] Manthiram A, Chung SH, Zu CX. Lithium–Sulfur Batteries: Progress and Prospects. Adv. Mater. 2015;27:1980-2006.

[6] Liu XR, Yuan YF, Liu J, et al. Utilizing solar energy to improve the oxygen evolution reaction kinetics in zinc-air battery, Nat Commun.2019;10:4767.

[7] Kobayashi T, Imade Y, Shishihara D, et al. All solid-state battery with sulfur electrode and thio-LISICON electrolyte. J Power Sources. 2008;182:621-5.

[8] Qi W, Shapter JG, Wu Q, Yin T, Gao G, Cui DX, Nanostructured anode materials for lithium-ion batteries: principle, recent progress and future perspectives. J Mater Chem A. 2017;5:19521-40.

[9] Goriparti S, Miele E,Angelis FD, Fabrizio ED, Zaccaria RP, Capiglia C. Review on recent progress of nanostructured anode materials for Li-ion batteries. J. Power Sources. 2014;257:421-443.

[10] Zhang YF. Wang PX, Zheng T, Li DM, Li GD, Yue YZ. Enhancing Li-ion battery anode performances via disorder/order engineering. Nano Energy. 2018;49:596-602.

[11] Yu LQ, Zhao SX, Wu X, Li WJ, Zhao EL, Wei GD, Lithium ion storage behaviors of $(100-x)V_2O_5-(x)P_2O_5$ glass as novel anode materials for Lithium Ion Battery. J Alloys Compd. 2019;810:151938.

[12] Du MY, Huang KK, Guo YM, et al. High specific capacity lithium ion battery cathode material prepared by synthesizing vanadate-phosphate glass in reducing atmosphere. J Power Sources. 2019;424: 91-9.

[13] Zhang YF, Glass anodes for lithium ion batteries: Insight from the structural evolution during discharging/charging. Int J Appl Glass Sci. 2020;00:1-13.

[14] Ličina V, Moguš-Milanković A, Reis ST, Day DE, Electronic conductivity in zinc iron phosphate glasses. J Non-Cryst Solids. 2007;353:4395-9.

[15] El-Desoky MM, Ibrahim FA, Hassaan MY, Effect of sulfur addition on the transport properties of semiconducting iron phosphate glasses. Solid State Sciences. 2011;13:1616-22.

[16] Austin IG, Mott NF. Polarons in crystalline and non-crystalline materials. Adv Phys. 1969; 18:41-102.

[17] Lee SS, Park CM, Facile conversion of waste glass into Li storage materials. Green Chem. 2019;21:1439-47.

[18] Qi SB, Li XY, Jiang ZJ, Zhang JY, Shan ZT, Zhang YF, Enhancing glass anode performance for lithium-ion batteries via crystallization. J Am Ceram Soc. In press.

[19] Kjeldsen J, Yue YZ, Bragatto CB, Rodrigues ACM. Electronic conductivity of vanadium-tellurite glass-ceramics. J. Non-Cryst. Solids. 2013;378:196-200.

[20] Pavic L, Skoko Z, Gajovic A, Su DS, Moguc-Milankovic A. Electrical transport in iron phosphate glass-ceramics. J Non-Cryst Solids. 2018;502:44-53.

[21] Zhang YF, Wang PX, Li GD, et.al. Clarifying the charging induced nucleation in glass anode of Li-ion batteries and its enhanced performances. Nano Energy. 2019; 57:592-9.

[22] Fan JH, Zhang YF, Li GD, Yue YZ. Tellurium nanoparticles enhanced electrochemical performances of TeO_2-V_2O_5-Al_2O_3 glass anode for Lithium-ion batteries. J Non-Cryst Solids. 2019;521:119491.

[23] Jiang ZJ, Zhao TY, Ren JJ, Zhang YF, Yue Y Z. NMR evidence for the charge-discharge induced structural evolution in a Li-ion battery glass anode and its impact on the electrochemical performances. Nano Energy. 2021;80:105589.

[24] Pavić L, Nikolić J, Graca MPF, et al. Effect of controlled crystallization on polaronic transport in phosphate- based glass- ceramics. Int J Appl Glass Sci. 2020;11:97-111.

[25] Nord AG. The crystal structure of iron(II) tetrametaphosphate, $Fe_2P_4O_{12}$, 1990;192:83-90.

[26] Yamashita T, Hayes P. Analysis of XPS spectra of Fe^{2+} and Fe^{3+} ions in oxide materials, Appl. Surf. Sci. 2008;254:2441-2449.

[27] Gao CW, Wang PX, Wang ZY, Kær SK, Zhang YF, Yue YZ. The disordering-enhanced performances of the Al-MOF/graphene composite anodes for lithium ion batteries, Nano Energy. 2019;104032.

[28] Chen X, Zhang NQ, Sun KN. Facile fabrication of CuO mesoporous nanosheet cluster array electrodes with super lithium-storage properties. J Mater Chem. 2012;22:13637.

[29] Barsoukov E, Macdonald JR. Impedance Spectroscopy: Theory, Experiment, and Applications, Second Edition. John Wiley & Sons, Inc., Hoboken, New Jersey; 2005.

[30] Liu JL, Jiang RR, Wang XY, Huang T, Yu AS. The defect chemistry of $LiFePO_4$ prepared by hydrothermal method at different pH values. J Power Sources. 2009;194:536-40.

[31] Molenda J, Ojczyk W, Marzec J. Electrical conductivity and reaction with lithium of $LiFe_{1-y}Mn_yPO_4$ olivine-type cathode materials. J Power Sources. 2007;174:689-94.

[32] Liu ZH, Yu Q, Zhao YL, et al. Silicon oxides: a promising family of anode materials for lithium-ion batteries. Chem. Soc. Rev., 2019;48:285-309.

[33] Levi MD, Aurbach D. Simultaneous measurements and modeling of the electrochemical impedance and the cyclic voltammetric characteristics of graphite electrodes doped with lithium. J. Phys. Chem. B 1997;101:4630-40

[34] Al-Assiri MS, El-Desoky MM. Correlation between nanostructural and electrical properties of barium titanate-based glass-ceramic nano-composites, J Alloy Compd. 2011;509:8937-43

[35] El-Desoky MM, Zayed HSS, Ibrahim FA, Ragab HS. Electrical conductivity improvement of strontium titanate doped lead vanadate glasses by nanocrystallization. Physica B. 2009;404:4125-31.

[36] Khalil MMI. Mixed polaronic-ionic conduction in lithium borate glasses and lass-ceramics containing copper oxide. Appl Phys. A. 2007;86:505-14.

Figure 1. particle size distributions of the glass powders milled of 50Fe50P glass in an agate mortar for 0.5h.
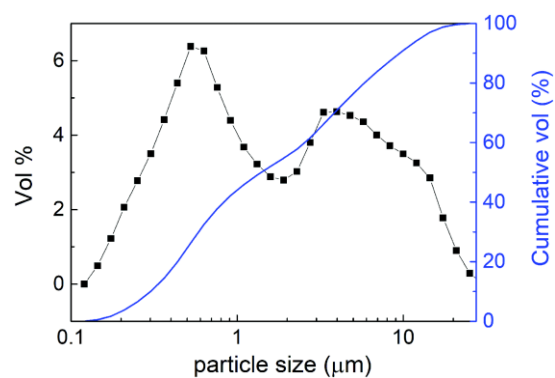
Figure 2. (a) The temperature dependence of DSC upscan curves of 50Fe50P glass and 50Fe50P subjected to treatment at 1118 K for 0.5 hour under air and reducing atmosphere, marked as A-0.5h and R-0.5h, respectively. (b) XRD patterns of A-0.5h and R-0.5h. SEM images of (c) A-0.5h and (d) R-0.5h. (e) Fe 2p XPS spectra of R-0.5h.
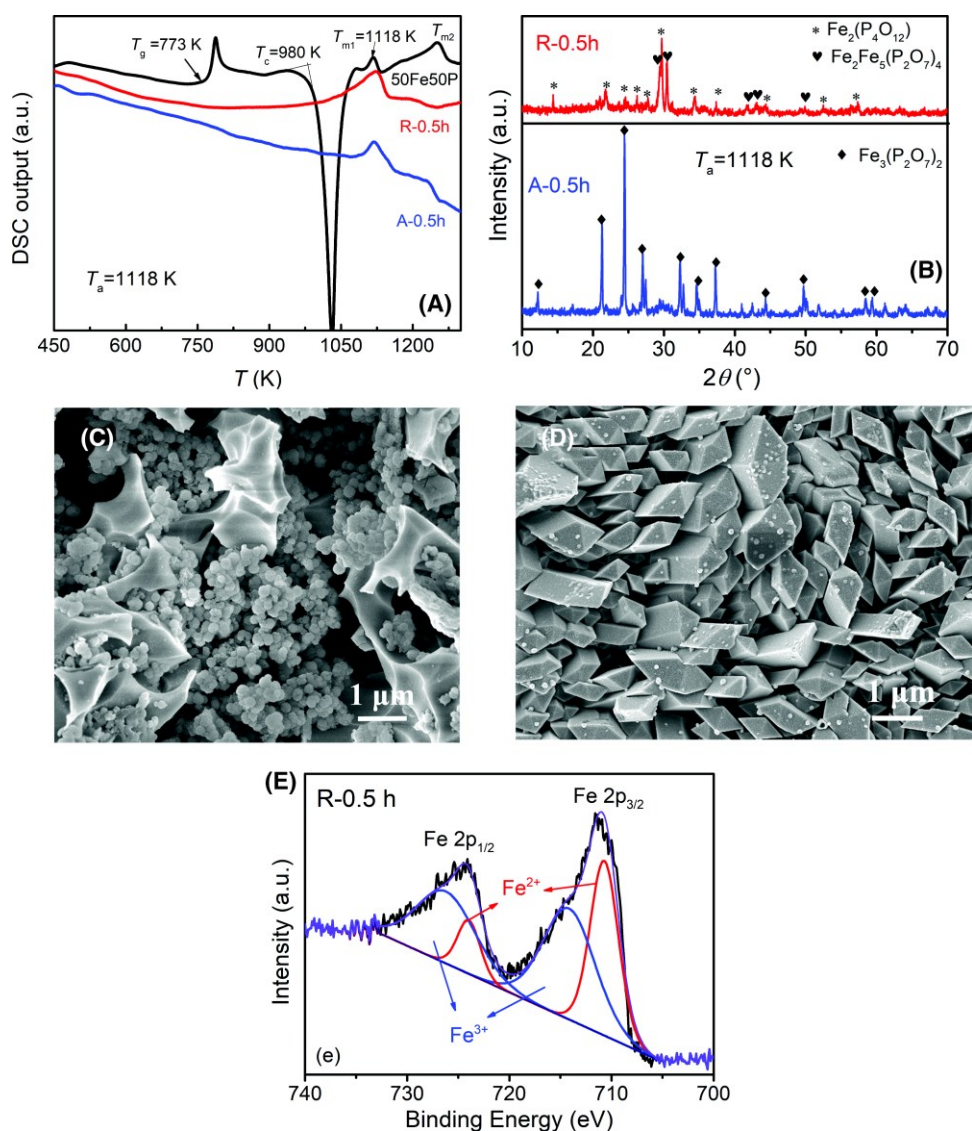
Figure 3. Electrochemical performances. (a) The cycling performances of 50Fe50P glass, A-0.5h and R-0.5h based anodes at 1 A g^{-1} and the coulomb efficiency of R-0.5h based anode. (b) Rate capability of 50Fe50P, A-0.5h and R-0.5h anodes. (c) EIS patterns of 50Fe50P, A-0.5h and R-0.5h anodes. Insets: the modeled equivalent circuit and the temperature dependence of electrical conductivity (log σ) for 50Fe50P, R-0.5h and A-0.5h, respectively. The solid lines are guide for eyes. (d) CV curves of R-0.5h based anode. Inset: Galvanostatic discharge/charge voltage profiles of R-0.5h based anode at different cycles.
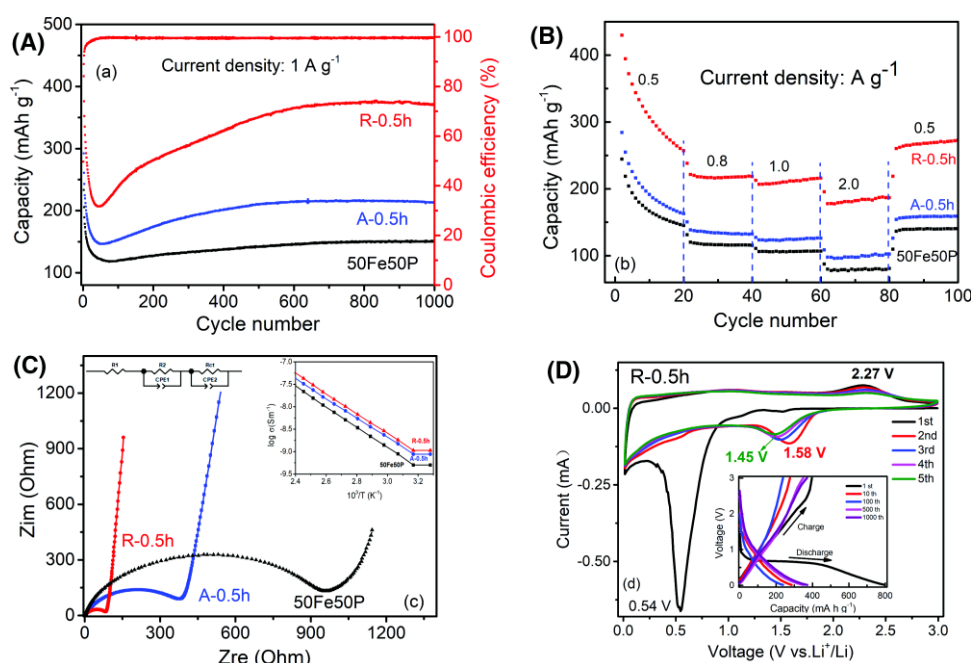
Figure 4. (a) XRD patterns and (b) the temperature dependence of the DSC curves of R-0.5h

sample before and after 1000 cycles. (c) SEM images of R-0.5h sample (c) before and (d)

after 1000 cycles. (e) Nyquist plots for R-0.5h anode before and after 1000 cycles.
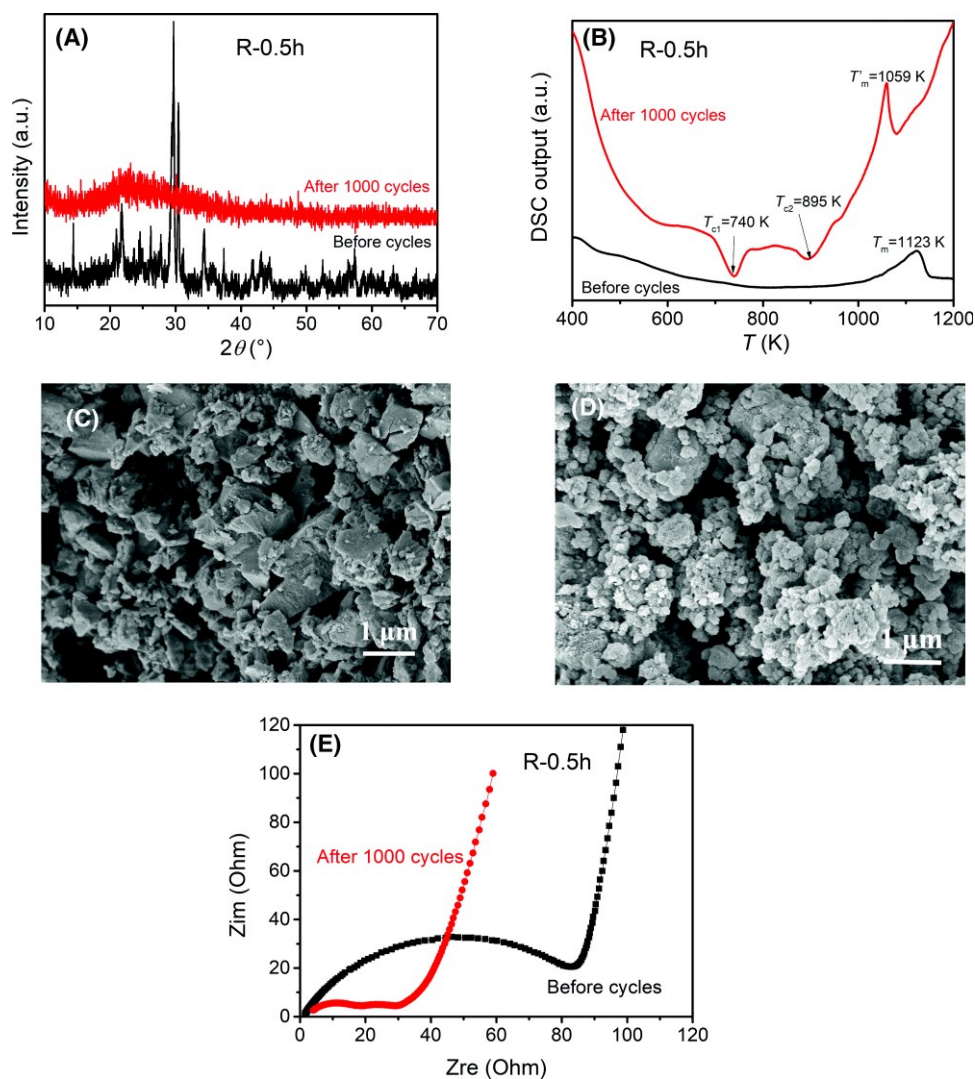
Figure 5 (a) The cycling performance and (b) EIS patterns of 50Fe50P glass heat treated at 1118 K for different time (t_a) under reducing atmosphere, i.e., R-0.16h, R-0.5h and R-4h. The inset of (a): the t_a dependence of the capacity of 50Fe50P anode at the end of 1000 cycles. The inset of (b): the enlarged EIS patterns.
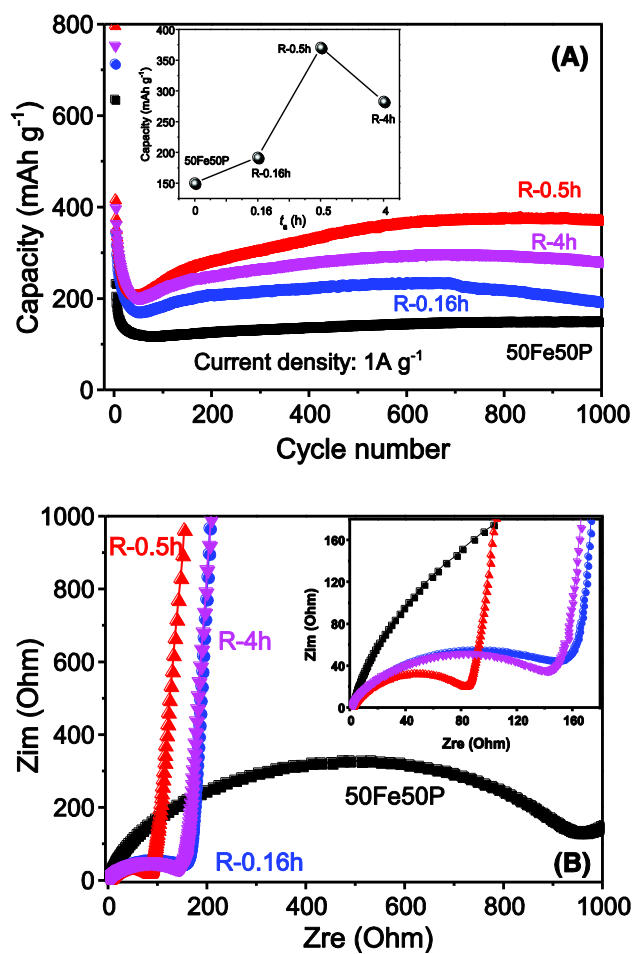
Figure 6 The XRD patterns of 50Fe50P glass heat treated at 1118 K for different time (t_a) under reducing atmosphere, namely, R-0.16h, R-0.5h and R-4h, respectively.